Multi-scale electrochemical reaction anode model for solid oxide fuel cells

Yuanyuan Xie, Xingjian Xue *

Department of Mechanical Engineering, University of South Carolina, Columbia, SC 29208, USA

ABSTRACT

A 2D axial-symmetrical model is developed for a button cell test system, integrating the detailed electrochemical elementary reactions with multiple transport processes. The model is validated using experimental polarization curves of the cell under different temperature conditions. Extensive simulations are performed to elucidate the complicated interactions between fuel/gas species, adsorbed/desorbed surface ions, elementary reactions, and their effects on the cell performance. Results indicate that the concentrations of surface adsorbed species of $O_{(s)}$, $OH_{(s)}$ and $H_2O_{(s)}$ ions presented at the anode/electrolyte interface are relatively high, while that of $H_{(s)}$ ion is relatively uniform within the entire anode. With increasing the operating temperature, the concentrations of surface adsorbed $O_{(s)}$, $OH_{(s)}$ and $H_2O_{(s)}$ ions at the anode/electrolyte interface are significantly improved, while the $H_{(s)}$ ion is slightly influenced. The adsorbed surface species $O_{(s)}$, $OH_{(s)}$ and $H_2O_{(s)}$ ions are very sensitive to the fuel compositions and cell voltage.

Published by Elsevier B.V.

1. Introduction

Solid oxide fuel cell (SOFC) is one of clean energy technologies that can convert the chemical energy of fuels into electricity in a highly efficient and environmentally benign manner [1,2]. The electrochemical reactions at solid/gas interface in porous electrodes play a very important role. Due to very aggressive operating conditions, direct measurement becomes difficult and the modeling technique has been widely used to study the complicated electrochemical reaction processes [3]. Usually, a set of conservation equations are used to describe the processes of heat transfer, fuel/gas species transport, and charge (ion and electron) migration. These processes are coupled together at solid/gas interface through Butler–Volmer equation [4,5]. In open literature, the Butler–Volmer equation is generally applied using bulk gas species, the detailed interim reaction species, which can improve the underlying mechanism understanding of electrochemical reactions, are usually neglected.

To overcome the limitations of the modeling method mentioned above, elementary reaction kinetic modeling is employed [6–9]. The elementary reaction models focus on the description of adsorption/desorption and surface reaction processes taking place at a local point, and is able to provide more precise electrochemical charge-transfer calculation through the balances of reaction species. It is usually assumed that such elementary reactions are identical across the entire porous electrodes. While this assumption can simplify the modeling and related computations, it is not consistent with the fact that the amplitude of such reactions could be different from one reaction site to another due to the limitations of mass transport processes. Therefore, there is a need to integrate the elementary reaction at each individual site with complicated fuel/gas transport processes [10–12].

The objective of this paper is to develop a mathematical model that can link the elementary reactions at individual sites and the complicated multiple transport processes in porous electrodes. The model is validated using the experimental data of a button cell. Comprehensive simulation studies are performed to investigate multi-scale interactions of electrochemical elementary reactions and multi-transport processes.

2. Model setup and governing equations

Shown in Fig. 1 is the schematic illustration of a button cell test stand. An anode-supported button cell Ni-YSZ/YSZ/LSM is mounted on one end of a large ceramic tube. The humidified hydrogen as a fuel is supplied to the anode electrode via a small ceramic tube. The surplus gas and product in the anode flow out through the large ceramic tube. The cathode electrode is exposed to the ambient air. A test furnace is used to control the temperature of the cell test stand. Such an experimental setting is employed as a physical base for mathematical model development. Due to the axial symmetry, two-dimensional computational domain is considered to model the button cell test system. The governing equations of the model include elementary reactions and multiple transport processes.

* Corresponding author. Tel.: +1 803 576 5598; fax: +1 803 777 0106.
E-mail address: Xue@cec.sc.edu (X. Xue).

Nomenclature

A	the Arrhenius parameter for the rate constants
c_i	concentration ($mol\,m^{-3}$)
$D_{m,k}$	ordinary diffusion coefficient ($m^2\,s^{-1}$)
D_{Kn}^{eff}	Knudsen diffusion coefficient ($m^2\,s^{-1}$)
D_i^{surf}	surface diffusivity of specie i ($m^2\,s^{-1}$)
D^T	thermal diffusion coefficient ($kg\,m^{-1}\,s^{-1}$)
E^0	the standard potential (V)
E^{act}	the thermal activation energy ($kJ\,mol^{-1}$)
F	Faraday's constant ($96,485\,C\,mol^{-1}$)
G	the Gibbs free energy (J)
i_F	Faradic current density ($A\,m^{-2}$)
k_f, k_b	the forward and backward reaction rate coefficients
K	permeability
K_{eq}	the equivalent thermal conductivity ($W\,m^{-1}\,K^{-1}$)
M_i	molecular weight of species i
m, n	the stoichiometric coefficients
p_i	the partial pressure of specie i
Q_H	the heat source term ($J\,mol^{-1}$)
r_i	the rate of elementary reaction i
R	universal gas constant ($8.314\,J\,mol\,K^{-1}$)
R_i	mass conservation source term of species i
R_n	the net reaction rate
l_{TPB}	three phase boundary length per unit volume ($m\,m^{-3}$)
T	temperature (K)
V	cell voltage (V)
x_i	molar fraction of specie i
z	the number of electrons
Γ	the available surface site density ($mol\,cm^{-2}$)
η_{act}	the activation overpotential (V)
θ_i	surface coverage of adsorbed specie i
ρ	density ($kg\,m^{-3}$)
$\sigma_{e,i}$	electronic/ionic charge conductivity ($S\,m^{-1}$)
σ_i^{surf}	the number of surface sites occupied by specie i
w_i	mass fraction of species i
μ	viscosity
ε	porosity
τ	tortuosity
ϕ	volume fraction of electronic conducting material

Subscripts

An	anode
Ca	cathode
El	electrolyte
Cl	channel
eff	effective
Ohm	Ohmic
elec/chem	Electrochemical/chemical

2.1. Elementary reactions

Electrochemical reactions involve multiple steps in the anode and strongly depend on the anode materials. For the Ni-YSZ composite anode, it is generally recognized that the following reaction processes are recognized when hydrogen is used as the fuel [9,13–15].

After hydrogen diffuses into porous anode, it interacts with nickel. The hydrogen can be adsorbed onto the surface of nickel as hydrogen atoms; the adsorbed hydrogen atoms can be desorbed off the nickel surface to form hydrogen molecules, i.e.,

$$H_2 + Ni \Leftrightarrow 2H_{(s)}$$
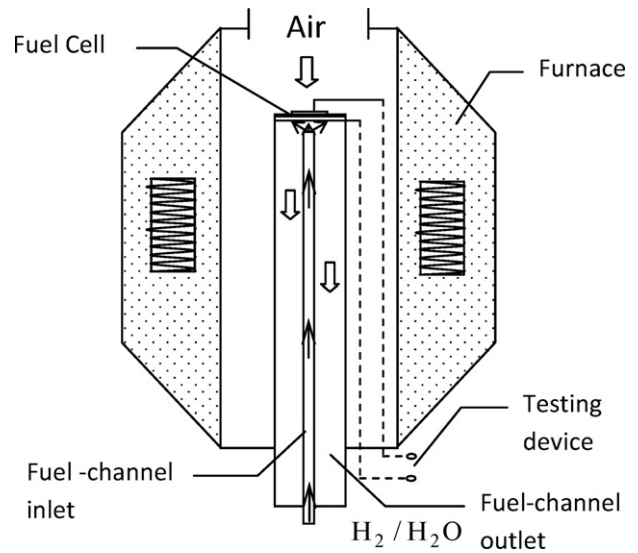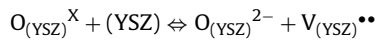
The reactions in two directions take place simultaneously until an equilibrium state is reached. The equilibrium state is dependent on the local multiple processes and thus the operating conditions of the cell.
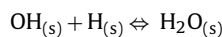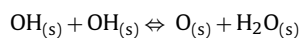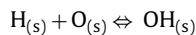
At the cathode side, oxygen ions $O_{(YSZ)}^{2-}$ are conducted toward the anode through the oxygen vacancies of electrolyte, e.g., YSZ,

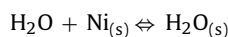$$O_{(YSZ)}^{X} + (YSZ) \Leftrightarrow O_{(YSZ)}^{2-} + V_{(YSZ)}^{\bullet\bullet}$$

where $O_{(YSZ)}^{X}$ is a lattice oxygen in YSZ and $V_{(YSZ)}^{\bullet\bullet}$ is an oxygen vacancy on YSZ surface. At three phase boundary (TPB) site, where nickel and YSZ as well as gas meet together, charge transfer reactions take place and several transfer pathways could occur at this site. It is recognized that incorrect predictions may be given by the two-step charge transfer mechanisms when the anode is polarized at high H_2O partial pressures [14]. Therefore, in the present elementary model a single-step oxygen-spillover process is assumed, i.e.,

$$O_{(YSZ)}^{2-} + Ni \Leftrightarrow O_{(s)} + (YSZ) + 2e_{(Ni)}^{-}$$
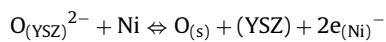
Here, the oxygen ions release electrons, forming oxygen atoms adsorbed onto the surface of YSZ. The electrons are released to the electronic conducting phase Ni. When the atomic oxygen $O_{(s)}$ on the surface of YSZ meets the adsorbed atomic hydrogen $H_{(s)}$ on the Ni surface at the TPB site, surface reactions take place. At this stage, there exist three possible surface reactions: the atomic hydrogen $H_{(s)}$ combines with atomic oxygen $O_{(s)}$, forming adsorbed hydroxyl $OH_{(s)}$; the hydroxyls may combine together to form water molecule and atomic oxygen; the $OH_{(s)}$ may further react with atomic hydrogen $H_{(s)}$ to form adsorbed water molecule,

$$H_{(s)} + O_{(s)} \Leftrightarrow OH_{(s)}$$

$$OH_{(s)} + OH_{(s)} \Leftrightarrow O_{(s)} + H_2O_{(s)}$$

$$OH_{(s)} + H_{(s)} \Leftrightarrow H_2O_{(s)}$$

In addition, the steam may also experience the adsorption/desorption processes on the surface of Ni,

$$H_2O + Ni_{(s)} \Leftrightarrow H_2O_{(s)}$$

Table 1
H_2/H_2O surface reaction mechanism [8,9,12,13].

Ni-surface		A	n	E
Adsorption/desorptionv (*f,b*)				
1	$H_2 + Ni_{(s)} + Ni_{(s)} \Leftrightarrow H_{(s)} + H_{(s)}$	$10^{-2}; 5.593 \times 10^{19}$	0; 0	0; 88.12
2	$H_2O + Ni_{(s)} \Leftrightarrow H_2O_{(s)}$	$1 \times 10^{-1}; 4.579 \times 10^{12}$	0; 0	0; 62.68
Surface reactions				
3	$O_{(s)} + H_{(s)} \Leftrightarrow OH_{(s)} + Ni_{(s)}$	$5 \times 10^{22}; 2.005 \times 10^{21}$	0; 0	97.9; 37.19
4	$OH_{(s)} + H_{(s)} \Leftrightarrow H_2O_{(s)} + Ni_{(s)}$	$3 \times 10^{20}; 2.175 \times 10^{21}$	0; 0	42.7; 91.36
5	$OH_{(s)} + OH_{(s)} \Leftrightarrow O_{(s)} + H_2O_{(s)}$	$3 \times 10^{21}; 5.423 \times 10^{23}$	0; 0	100; 209.37
Ni/YSZ-surface (charge transfer reactions)		A^0	α	E
6	$O_{(YSZ)}^X + (YSZ) \Leftrightarrow O_{(YSZ)}^{2-} + V_{(YSZ)}^{\bullet\bullet}$	1.6×10^{22}	0	90.9
7	$O_{(YSZ)}^{2-} + Ni_{(s)} \Leftrightarrow O_{(s)} + (YSZ) + 2e_{(Ni)}^-$	4.9×10^{-6}	0.5	*c*

Rate constant of Arrhenius equation written as: $k = AT^n \exp(-E/RT)$, the unit of E is kJ mol^{-1}, *c* – calculated or estimated from references.
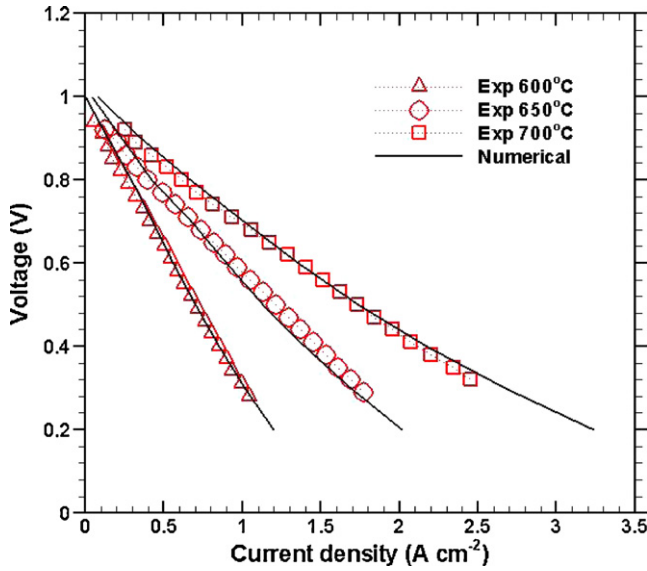

Fig. 2. Comparisons between experimental and numerical data.

Table 1 summarizes the elementary reactions in Ni/YSZ composite anode. The electrochemical reactions in the anode can be represented with a generic formula [5],

$$\sum_i^n n_i Ra_i \Leftrightarrow \sum_j^m m_j Pu_j + ze^- \qquad (1)$$

where Ra is the reactant, Pu is the product, n_i and m_j are the stoichiometric factors for the reactants and products, respectively, z is the number of electrons. Using Arrhenius formula, the forward and backward reaction rate coefficient k_f and k_b can be calculated as [7,9],

$$k_f = AT^n \exp\left(\frac{-E^{act}}{RT}\right) \exp\left(\alpha \frac{zF}{RT}\eta\right) \qquad (2)$$

$$k_b = AT^n \exp\left(\frac{-E^{act}}{RT}\right) \exp\left(-(1-\alpha)\frac{zF}{RT}\eta\right) \qquad (3)$$

where E^{act} is the thermal activation energy, η is the electrical potential difference between the reactants and products. The net reaction rate R_n can be determined as,

$$R_n = k_f \prod_i [Ra_i]^{n_i} - k_b \prod_j [Pu_j]^{m_j} \qquad (4)$$

Then the elementary kinetic description of charge transfer can be formulated as,

$$i_{F,an} = Fl_{TPB} \sum zR_n \qquad (5)$$

where $i_{F,an}$ is the source of the faradic current derived from electrochemical reactions in the anode; l_{TPB} is the volume-specific TPB length of the composite anode. Because the electroactive species involved in the charge-transfer reactions are surface-adsorbed intermediates, to study their variations of spatial distribution, the surface coverage θ_is are calculated through the surface diffusion process [6,12],

$$\frac{\sigma_i^{surf}}{\Gamma} R_i = -\nabla \cdot (D_i^{surf} \nabla \theta_i), \quad \theta_i = \frac{\sigma_i^{surf} c_i}{\Gamma} \qquad (6)$$

where σ_i^{surf} is the number of surface sites occupied by species i; Γ is the area-specific density of adsorption site (mol cm^{-2}); D_i^{surf} is the surface diffusivity of species i; c_i is the concentration of surface species i. The elementary reactions are influenced by the local species concentrations through surface diffusion process, and the species concentrations are influenced by not only the local elementary reactions but also the complicated transport processes in porous electrodes. To study these coupling effects, the elementary reactions are linked to macro-scale transport processes.

Since the cathode has much simple elementary reaction steps, the equation from [9] is used to describe the oxygen reduction process,

$$i_{F,ca} = i_{ca}^* \frac{(p_{O_2}/p_{O_2}^0)^{0.25}}{1 + (p_{O_2}/p_{O_2}^0)^{0.5}} \left(\exp\left(\frac{0.5F\eta_{act}}{RT}\right) - \exp\left(-\frac{0.5F\eta_{act}}{RT}\right)\right) \qquad (7)$$

where i_{ca}^* is a free parameter used to fit the model predictions with experimental data; $\rho_{O_2}^0 = 4.9 \times 10^8 \exp(-2 \times 10^5/RT)$; p_{O_2} is the partial pressure of local oxygen; η_{act} is the activation overpotential $\eta_{act} = \eta - \eta_{eq}$, $\eta = V_e - V_i$ and η_{eq} can be determined using the reactants and products of elementary reactions,

$$\eta_{eq} = \frac{\Delta G}{zF} + \frac{RT}{zF} \ln\left(\frac{\prod_j [Pu_j]^{m_j}}{\prod_i [Ra_i]^{n_i}}\right) \qquad (8)$$

here ΔG is the Gibbs free energy of the reaction. Considering that the hydrogen electro-oxidation pathway is dominant, Eq. (8) can be simplified as,

$$\eta_{eq} = E^0 + \frac{RT}{2F} \ln\left(\frac{p_{H_2} p_{O_2}^{0.5}}{p_{H_2O}}\right) \qquad (9)$$
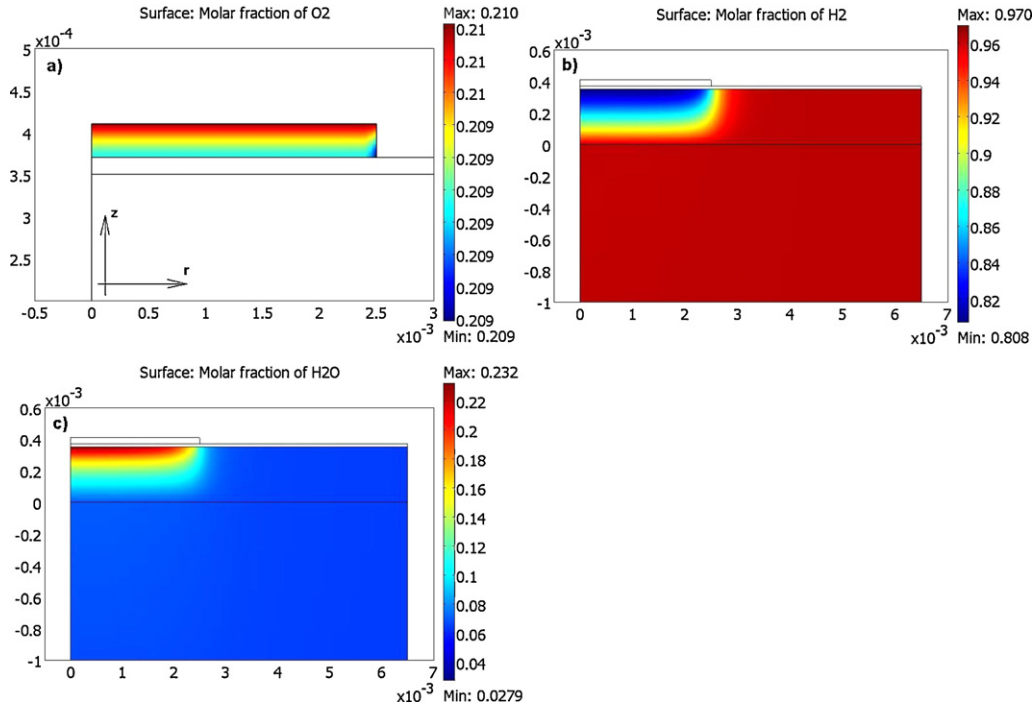
Fig. 3. The molar fraction distribution of bulk gas species within electrodes: (a) oxygen, (b) hydrogen and (c) steam.

2.2. Transport processes

In addition to electrochemical elementary reactions, SOFCs also include very complicated transport processes, such as fuel/gas transport in porous electrodes, charge transport through material backbone, as well as heat transfer. The mass and charge transport processes are coupled together at reaction sites of porous electrodes through elementary reactions. To elucidate these complicated interactions, the multi-transport processes are further modeled.
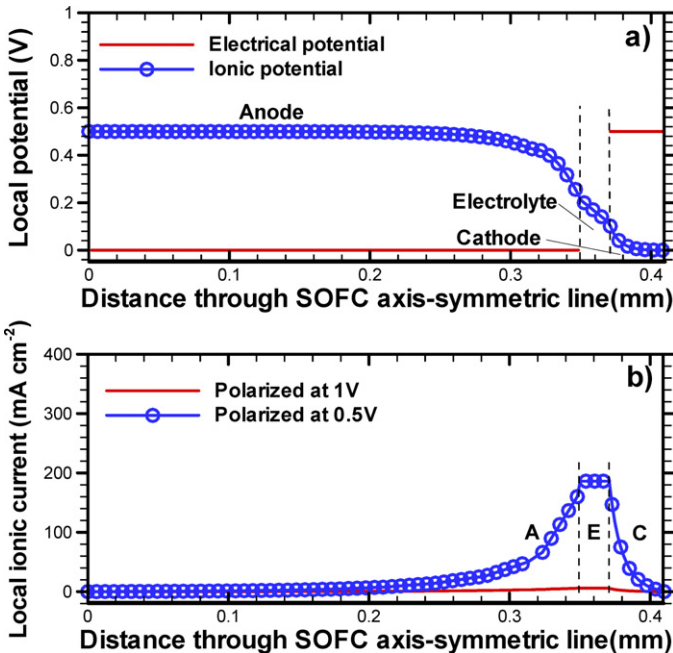

Fig. 4. The distribution of local potential and current along cell axis-symmetric line: (a) local potential and (b) local ionic current.

2.2.1. Charge conservation

The charge conservation includes both ionic and electronic transport processes and can be formulated using generic Ohm's law

$$-\nabla \cdot (\sigma_n^{\text{eff}} \nabla V_n) = \pm i_F; \quad n = e, i \tag{10}$$

where V_n is the potential; σ_n^{eff} is the effective conductivity; e/i represent electron and ion respectively; i_F is the volume-specific faradic current in electrodes. For composite electrodes, e.g., Ni/YSZ, the conductivity can be further calculated as $\sigma_e^{\text{eff}} = \phi(1-\varepsilon)\sigma_e/\tau$, $\sigma_i^{\text{eff}} = (1-\phi)(1-\varepsilon)\sigma_i/\tau$, here ε is the porosity, τ is the tortuosity, and ϕ is the volume fraction of electronic conducting phase in the electrode.

2.2.2. Mass conservation

Since the multi-species fuel/gas are involved, the Stefan-Maxwell equation is employed to describe multi-species transport in both porous electrodes as well as fuel/gas supply channel,

$$\nabla \cdot \left(-\rho w_m \sum_k D_{m,k}^{\text{eff}} \left(\nabla x_k + (x_k - w_k)\frac{\nabla p}{p} \right) - D^T \frac{\nabla T}{T} \right)$$
$$+ \rho v \cdot \nabla w_m = R_i \tag{11}$$

where the subscripts m and k stand for different gas species; w the mass fraction; $D_{m,k}^{\text{eff}}$ is the effective diffusion coefficient; R_i is the source term. The effective diffusion coefficient $D_{m,k}^{\text{eff}}$ is determined by combining molecular diffusion in large pores and Knudsen diffusion in small pores comparable to the molecular mean-free path,

$$D_{m,k}^{\text{eff}} = \left(\frac{\tau}{\varepsilon D_{m,k}} + \frac{1}{D_{\text{Kn}}^{\text{eff}}} \right)^{-1} \tag{12}$$

2.2.3. Momentum conservation

To describe the momentum conservation in the fuel/gas supply channel and porous electrodes, the weakly compressible Brinkman

Table 2
Reaction rates and source terms.

Reaction rate	Reaction source term	Energy source term
$r_1 = k_{1,f}[H_2] - k_{1,b}[H_{(s)}]^2$	$R_{H_2} = -r_1$	$R_{Ca} = Q_{Ohm} + Q_{elec/chem}$
$r_2 = k_{2,f}[H_2O] - k_{2,b}[H_2O_{(s)}]$	$R_{H_2O} = -r_2$	$R_{El} = Q_{Ohm}$
$r_3 = k_{3,f}[H_{(s)}][O_{(s)}] - k_{3,b}[OH_{(s)}]$	$R_{H(s)} = 2r_1 - r_3 - r_4$	$R_{An} = Q_{Ohm} + Q_{elec/chem}$
$r_4 = k_{4,f}[OH_{(s)}][H_{(s)}] - k_{4,b}[H_2O_{(s)}]$	$R_{OH_{(s)}} = r_3 - r_4 - 2r_5$	$R_{Cl} = 0$
$r_5 = k_{5,f}[OH_{(s)}]^2 - k_{5,b}[O_{(s)}][H_2O_{(s)}]$	$R_{H_2O_{(s)}} = r_1 - r_4 + r_5$	

Table 3
Boundary conditions.

	Cathode/channel interface	Cathode/electrolyte interface	Anode/electrolyte interface	Channel/anode interface	Fuel channel
Ionic charge balance	Insulation	Continuity	Continuity	Insulation	N/A
Electronic charge balance	Specified voltage	Insulation	Insulation	0	N/A
Mass	O_2/N_2 mass fractions	Insulation	Insulation	Continuity	H_2/H_2O mass fractions
Momentum	Pressure	Wall	Wall	Continuity	Flow rate, pressure
Energy	Temperature	Continuity	Continuity	Continuity	Temperature

equation and the Darcy's law are used respectively,

$$\rho(v \cdot \nabla)v = \nabla \cdot \left[-pI + \eta(\nabla u + (\nabla u)^T) - \left(\frac{2\eta}{3} - \kappa_{dv} \right)(\nabla \cdot u)I \right] + F \tag{13}$$

$$-\frac{K}{\mu}\nabla P = v \tag{14}$$

where μ is the viscosity of fuel/gas, K is the permeability and can be formulated as [16]:

$$K = \frac{\varepsilon^3 d_p^2}{150(1-\varepsilon)^2} \tag{15}$$

Here d_p is the average particle diameter of porous electrodes.

2.2.4. Energy conservation
The energy conservation in porous electrodes is described as,

$$-\nabla \cdot (K_{eq}\nabla T) = Q_H - C_L u \cdot \nabla T \tag{16}$$

where $K_{eq} = \beta K_L + (1 - \beta)K_P$ is the equivalent thermal conductivity, K_L is the effective heat conductivity of liquid phase, K_P is the heat conductivity of solid phase, β is the volume fraction of liquid phase; C_L is the effective volumetric heat capacity; Q_H is the general heat source term and can be described as $Q_H = Q_{elec/chem} + Q_{Ohm}$, which includes the chemical/electrochemical reaction heat ($Q_{elec/chem}$) and ohmic resistance induced heat generation ($Q_{Ohm} = -i \cdot \eta = i^2R$). Table 2 summarizes the relevant heat generation mechanisms and the corresponding mathematical expressions according to the equilibrium of chemical/electrochemical reactions.
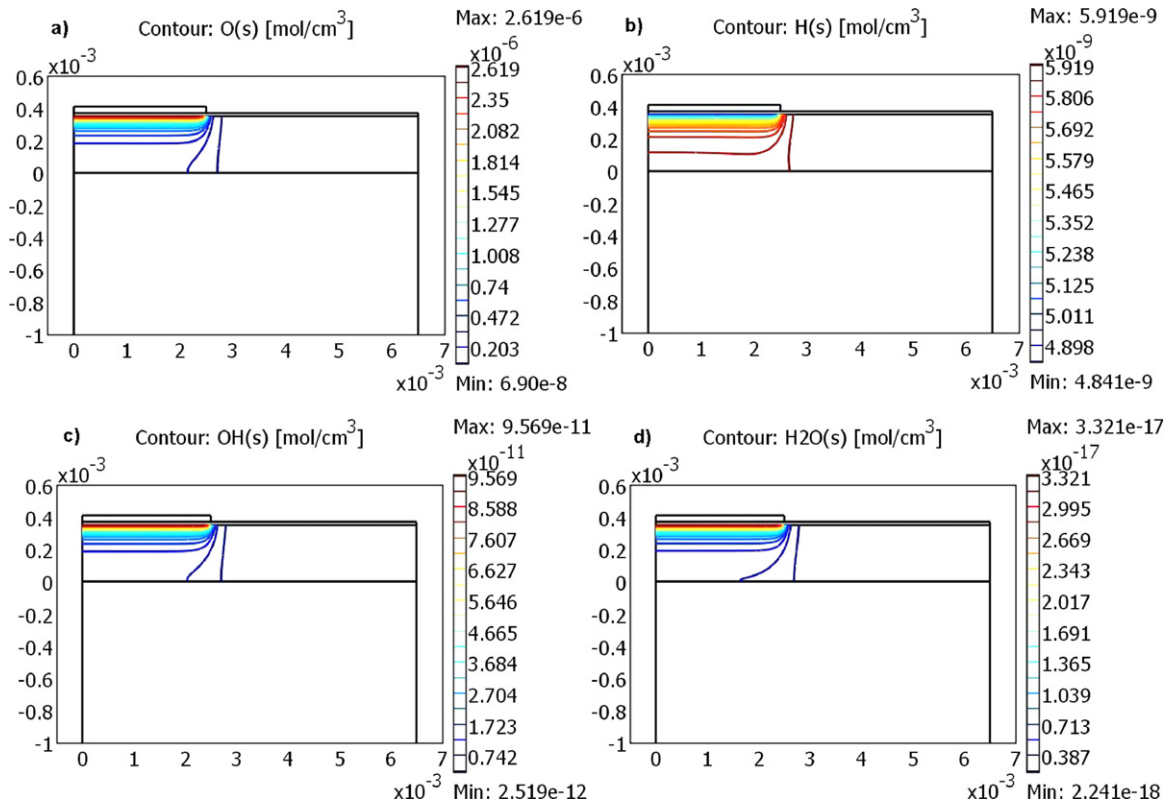

Fig. 5. The concentration distribution of adsorbed surface species within the anode: (a) $O_{(s)}$, (b) $H_{(s)}$, (c) $OH_{(s)}$, and (d) $H_2O_{(s)}$.
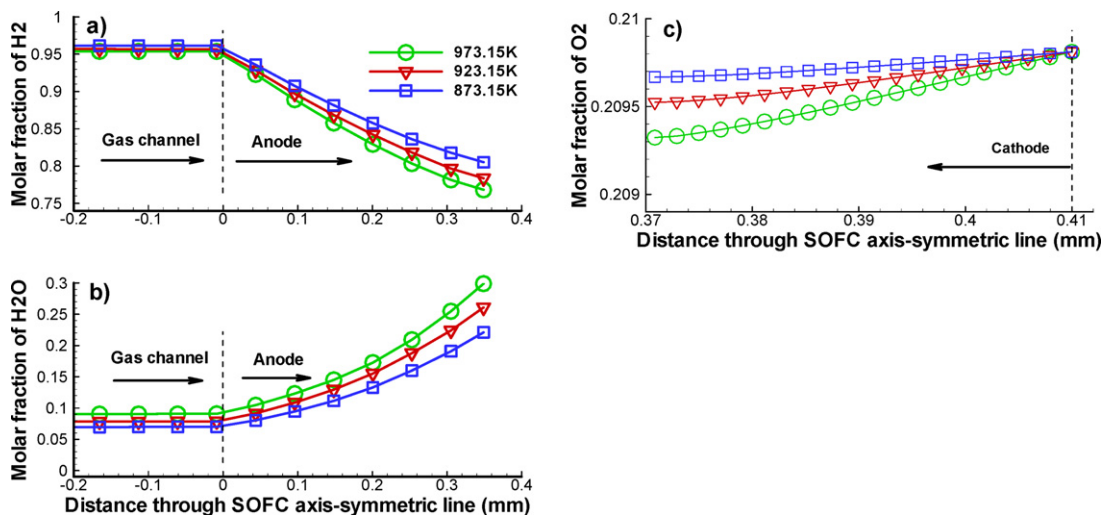
Fig. 6. Effects of operating temperature on the bulk fuel species distribution along cell axis-symmetric line: (a) hydrogen, (b) steam, and (c) oxygen.

2.3. Boundary conditions

To solve the equations of elementary reactions and multiphysics transport processes, boundary conditions are needed. According to the experimental setup, the boundary conditions are summarized in Table 3.

3. Solution algorithm and model validation

The mathematical model is solved using COMSOL MULTIPH-SICS V4.0. The model parameters are provided in Table 4. For a specified cell voltage at the cathode electrode boundary, the distributions of various parameters are calculated. Accordingly, the average cell current density is obtained. The cell polarization curve is then obtained by specifying a series of cell voltages and calculating the corresponding average cell current density. And the species associated with multi-physicochemical processes are calculated at each of the specified voltage conditions.

The model is validated using experimental polarization curves, where the humidified hydrogen (97% hydrogen and 3% vapor) is

used as the fuel and ambient oxygen is used as the oxidant. The cell polarization curve is obtained at temperature 600 °C, 650 °C and 700 °C respectively. As shown in Fig. 2, the model predictions match with experimental data reasonably well. The validated model is then used for further simulation studies.

4. Results and discussion

4.1. Distributions of fuel/gas and local potential/current

Fig. 3 shows the molar fraction distributions of hydrogen, vapor, and oxygen, where the furnace temperature is 973 K and the cell voltage is 0.5 V. The molar fraction of hydrogen shows little variation in fuel supply tube, but decreases in the anode toward the anode/electrolyte interface. The variation is well aligned with the size of the cathode. The molar fraction of vapor shows opposite trend and increases toward the anode/electrolyte interface. The resulting such distributions are due to the fact that the electrochemical reactions in the anode consume hydrogen while producing water molecules. Similarly, on the cathode side,
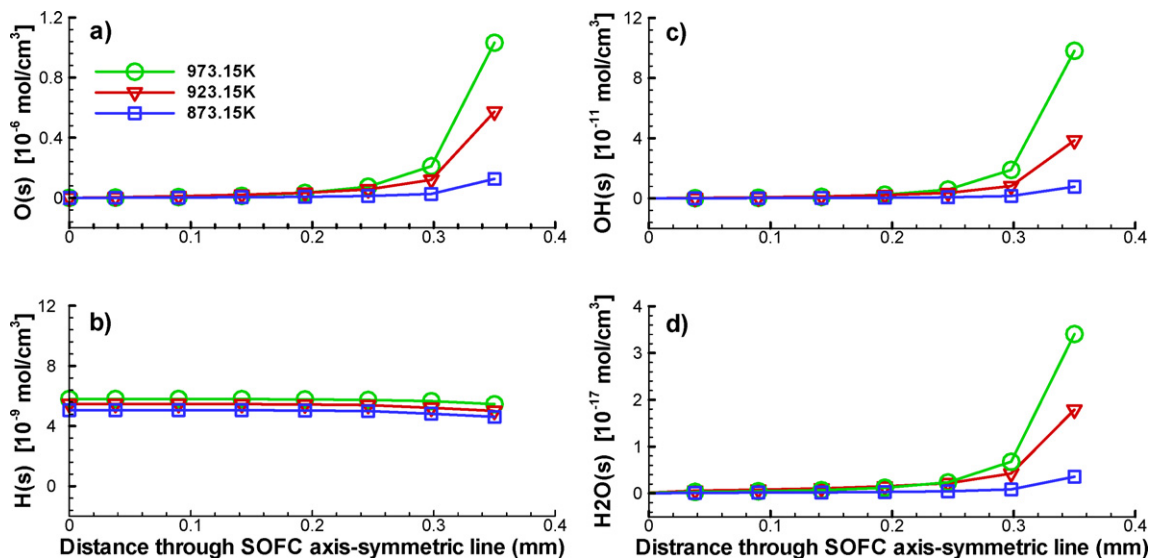

Fig. 7. Effects of operating temperature on the adsorbed species along cell axis-symmetric line: (a) $O_{(s)}$, (b) $H_{(s)}$, (c) $OH_{(s)}$, and (d) $H_2O_{(s)}$.
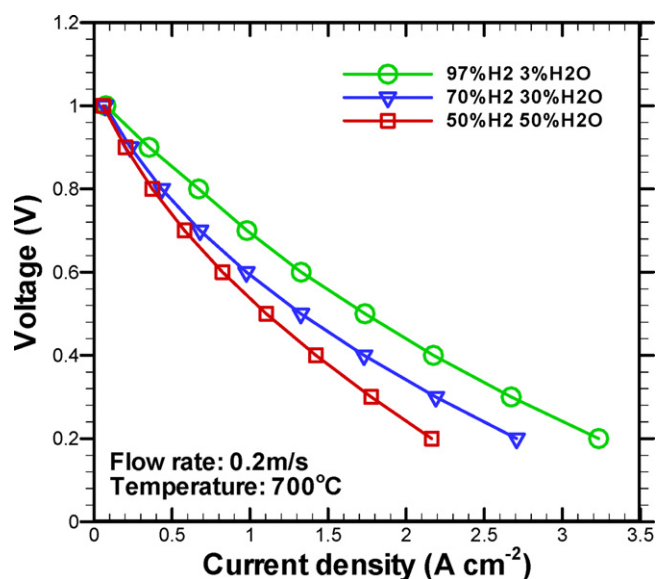
Fig. 8. Effects of fuel compositions on the cell performance.

Table 4
Operation parameters [8,17,18].

	Value	Units
Cathode layer thickness, radius	$4 \times 10^{-5}, 2.5 \times 10^{-3}$	m
Electrolyte layer thickness, radius	$2 \times 10^{-5}, 6.5 \times 10^{-3}$	m
Anode layer thickness, radius	$3.5 \times 10^{-4}, 6.5 \times 10^{-3}$	m
Inlet fuel channel radius, wall radius	$1 \times 10^{-3}, 1.5 \times 10^{-3}$	m
Outlet fuel channel radius	6.5×10^{-3}	m
Faraday constant	96485	C mol^{-1}
Gas constant	8.314	J mol^{-1} K^{-1}
Operating temperature	700	°C
Pressure	1	atm
Anode ionic conductivity	$3.34 \times 10^4 \exp(-10300/T)$	S m^{-1}
Cathode ionic conductivity	$3.34 \times 10^4 \exp(-10300/T)$	S m^{-1}
Anode electronic conductivity	2×10^6	S m^{-1}
Cathode electronic conductivity	$42 \times 10^6 \exp(-1150/T)/T$	S m^{-1}
Electrolyte ionic conductivity	$3.34 \times 10^4 \exp(-10300/T)$	S m^{-1}
Porosity (ε)	0.4	1
Particle diameter	2×10^{-6}	m
Tortuosity	$[(3 - \varepsilon)/2]^{0.5}$	1
Permeability	$\varepsilon^3 d^2 / 150(1 - \varepsilon)^2$	1
Inlet velocity	0.2	m s^{-1}
Surface site density of Ni	6.1×10^{-9}	mol cm^{-2}
Specific three-phase boundary length	1.8×10^{12}	m m^{-3}

the molar fraction of oxygen shows a slight decrease toward the cathode/electrolyte interface, in which the oxygen is consumed by electrochemical reactions.

The electrical/ionic potentials and ionic current distribution are examined along the axis-symmetric line. As shown in Fig. 4a, when the cell voltage is set at 0.5 V, the electrical potential of the cathode and anode remains at 0.5 V and 0 V respectively and does not show any gradient along the axial-symmetric line. The ionic potential is about 0.5 V in the anode and approaches to zero in the cathode. Obvious gradients of ionic potential exist across the electrolyte. The current distribution along the axial-symmetric line is shown in Fig. 4b. Clearly the ionic current reaches the highest value within the electrolyte, which is consistent with ionic potential distributions. This observation suggests that the electrochemical reactions mainly occur near the electrode/electrolyte interface. When the specified cell voltage increases to 1 V, the ionic current significantly decreases as shown in Fig. 4b.
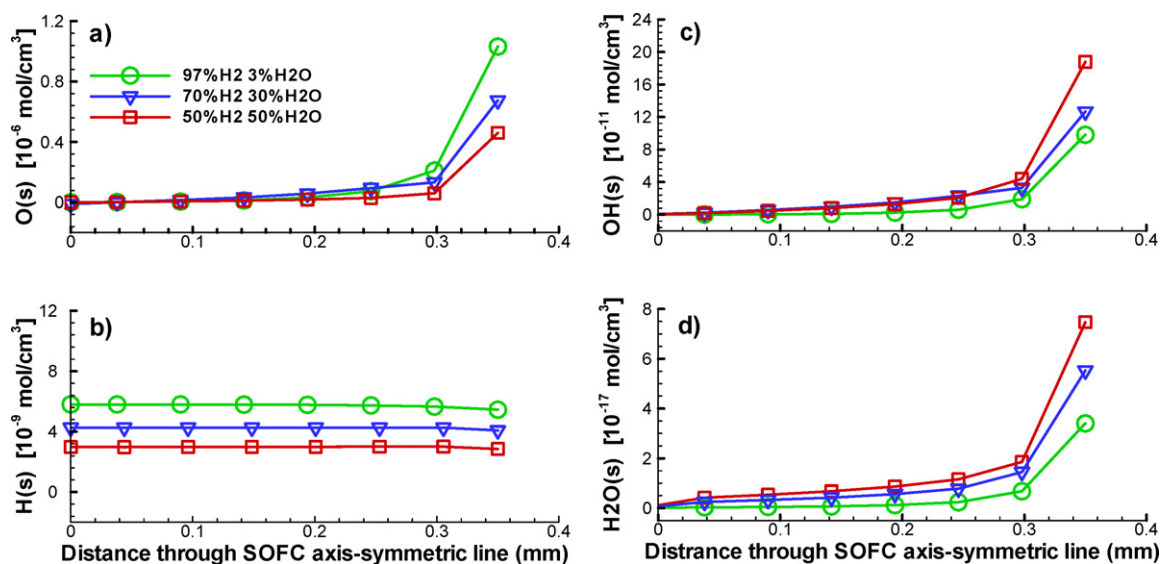
4.2. Surface species distribution within the anode

The adsorbed surface species such as $O_{(s)}$, $H_{(s)}$, $OH_{(s)}$, $H_2O_{(s)}$ are very important intermediates influencing the electrochemical reactions at TPB sites in the anode. As shown in Fig. 5, the concentration of species $H_{(s)}$ increases from the electrolyte/anode interface toward the anode/channel interface, while the concentrations of other species, e.g., $O_{(s)}$, $OH_{(s)}$, $H_2O_{(s)}$, decrease. One may also notice that the concentration of species $H_{(s)}$ is relatively uniform within the anode, however, those of the species $O_{(s)}$, $OH_{(s)}$, $H_2O_{(s)}$ show relatively large gradients with the highest concentrations at the electrolyte/anode interface. It is generally recognized that Ni is a very active catalyst and uniformly distributed within the composite anode. As a result, the $H_{(s)}$ ions are generated throughout the entire anode, leading to the relatively uniform distribution of species $H_{(s)}$. The species $O_{(s)}$ is generated from $O_{(YSZ)}^{2-}$ ions conducted from the cathode side. The species $O_{(s)}$ is consumed at the anode/electrolyte interface and keeps being consumed within the anode, resulting in the decrease of spatial concentration from the anode/electrolyte
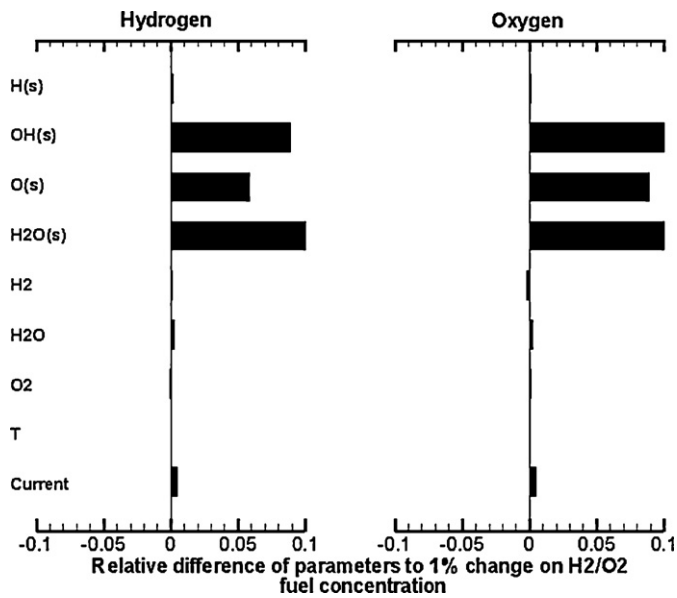

Fig. 9. Effects of fuel composition on the adsorbed species along cell axis-symmetric line: (a) $O_{(s)}$, (b) $H_{(s)}$, (c) $OH_{(s)}$, and (d) $H_2O_{(s)}$.

Fig. 10. Sensitivity of species and cell parameters with respect to fuel compositions. The parameter values are recorded at the intersecting point between electrode/electrolyte interface and cell axial-symmetric line.

interface toward the anode/channel interface. The OH$_{(s)}$ ions and H$_2$O$_{(s)}$ ions have much lower concentrations compared with those of O$_{(s)}$ and H$_{(s)}$ ions, and their highest concentrations occur in the area close to the anode/electrolyte interface. These observations suggest that most of the surface reactions take place around the anode/electrolyte interface.

4.3. Effects of operating temperatures

Experimental results show that the cell performance is significantly affected by the operating temperatures (Fig. 3). To study the

corresponding species transport processes under different temperatures, the modeling analysis is further performed. Fig. 6 shows the distributions of fuel/gas along the axial-symmetrical line of the cell at temperature 873 K, 923 K, 973 K, respectively. Essentially, the molar fractions of hydrogen and oxygen decrease from the channel/electrode interface toward the electrolyte/electrode interface. The gradients of hydrogen and oxygen molar fractions increase with increasing operating temperature, indicating that more hydrogen and oxygen are consumed in higher operating temperatures. On the other hand, the concentration of vapor (H$_2$O) shows opposite trend, and the production of H$_2$O increases with increasing the operating temperature.

Fig. 7 shows the distributions of adsorbed surface species within the anode along the axial-symmetrical line of the cell at temperature 873 K, 923 K, 973 K, respectively. The species H$_{(s)}$ ion shows relatively uniform distribution and a slight variation under different temperatures. The concentrations of other three species O$_{(s)}$ ion, OH$_{(s)}$ ion, and H$_2$O$_{(s)}$ ion are very low but increase significantly approaching the anode/electrolyte interface, and increase with increasing the operating temperatures. These observations again indicate that the electrochemical reactions in the anode mainly take place near the anode/electrolyte interface, even though the composite anode is employed. One also can see that the concentrations of involved OH$_{(s)}$ ions and H$_2$O$_{(s)}$ ions are much lower than those of H$_{(s)}$ ions and O$_{(s)}$ ions.

4.4. Effects of fuel compositions

The effects of fuel composition on SOFC performance have been widely investigated through modeling techniques in open literature, however the elementary reactions are generally neglected. As a result, the adsorbed surface intermediates are not considered. In this section, the surface electrochemistry details are further studied. Fig. 8 shows the polarization performance of the cell under different fuel composition conditions. Obviously, larger hydrogen fraction in fuel supply leads to better cell performance. Fig. 9
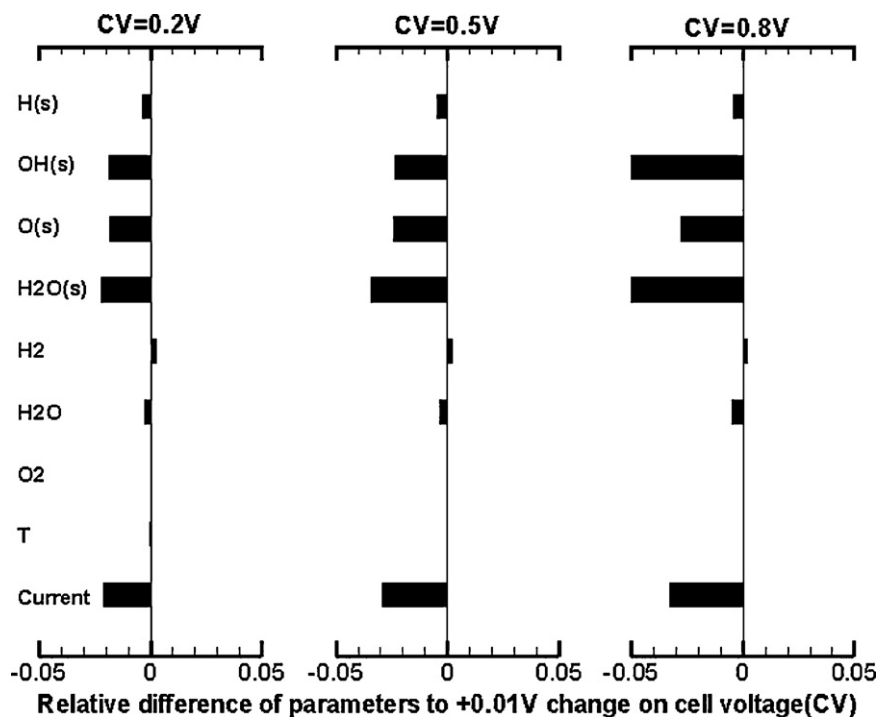

Fig. 11. Sensitivity of species and cell parameters with respect to cell voltages. The parameter values are recorded at the intersecting point between electrode/electrolyte interface and cell axial-symmetric line.

shows the corresponding distributions of adsorbates along the axial-symmetrical line of the cell. Basically, the concentration of adsorbed $H_{(s)}$ ion increases with increasing hydrogen fraction in the fuel, and are relatively uniform. The concentration of adsorbed species $O_{(s)}$ increases near the anode/electrolyte interface with increasing hydrogen fraction in the fuel, while those of adsorbed species $OH_{(s)}$ ion and $H_2O_{(s)}$ decrease. When hydrogen fraction in the fuel is low, less $H_{(s)}$ ions are generated. This leads to low chemical potential for $O_{(s)}$ production. As a result, the electrochemical reaction rate reduces and the cell performance decreases. On the other hand, when more $H_2O_{(s)}$ and $OH_{(s)}$ ions are generated by higher bulk H_2O concentration, it can raise the backward rate of surface chemical reactions. Accordingly the electrochemical reaction rate will also reduce. Therefore, the effect of fuel composition on the cell performance depends on not only the reactant fuels but also the product species generated.

To study the sensitivity of the generated intermediate species and other cell parameters with respect to the variations of supplied hydrogen and oxygen, the simulations are run by adding 1% more hydrogen and oxygen to the anode and cathode respectively. Fig. 10 shows the corresponding variations of various parameters at the anode/electrolyte interface. It is clearly seen that the surface adsorbed species $O_{(s)}$, $H_2O_{(s)}$, and $OH_{(s)}$ ions are very sensitive to the composition changes of fuel/gas. This result indicates that increasing fuel/gas concentrations can effectively improve the chemical potentials for the surface intermediate species productions and surface electrochemical reactions.

4.5. Effects of cell voltage

The sensitivities of various parameters with respect to the variation of cell voltage are also studied. Fig. 11 shows parameter variations at the anode/electrolyte interface when the cell voltage increases from 0.2 V, 0.5 V, and 0.8 V to 0.21 V, 0.51 V, and 0.81 V respectively. The cell current and three adsorbed surface species $O_{(s)}$, $H_2O_{(s)}$, and $OH_{(s)}$ ions demonstrate relatively high sensitivities. The concentrations of adsorbed surface species $H_{(s)}$ and the bulk H_2 and H_2O show slight variations. The variations of bulk O_2 and the cell temperature are negligible. One may also see that relatively high sensitivity is obtained at cell voltage 0.8 V, particularly for adsorbed surface species $OH_{(s)}$ and $H_2O_{(s)}$. At high cell voltage conditions, the consumed hydrogen and oxygen are low. As a result, their concentrations are maintained at relatively high level. Accordingly, high chemical potentials are generated for adsorbate productions.

5. Conclusion

A 2D-axial-symmetrical SOFC model is developed using an anode-supported Ni-YSZ/YSZ/LSM button cell test system as the physical base, in which the humidified hydrogen is used as the fuel and ambient air as the oxidant. The model considers the elementary reactions at TPB sites in the anode and multiple transport processes. The elementary reactions are linked with multi-transport processes in a coherent way. The model is validated with experimental data. Simulation results indicate that very complicated interactions exist among fuel/gas transport in porous electrodes, adsorbed/desorbed species on the surface of porous electrodes, and charge transport through solid backbone, as well as elementary reactions. The concentrations of surface adsorbed species of $O_{(s)}$, $OH_{(s)}$ and $H_2O_{(s)}$ ions presented at the anode/electrolyte interface are relatively high, while that of $H_{(s)}$ ion is relatively uniform within the entire anode. With increasing the operating temperature, the concentrations of surface adsorbed $O_{(s)}$, $OH_{(s)}$ and $H_2O_{(s)}$ ions at the anode/electrolyte interface are significantly improved, while that of $H_{(s)}$ ion is slightly influenced. The adsorbed surface species $O_{(s)}$, $OH_{(s)}$ and $H_2O_{(s)}$ ions are very sensitive to the variations of the supplied hydrogen and oxygen as well as the cell voltage.

References

[1] D.J.L. Brett, A. Atkinson, N.P. Brandon, S.J. Skinner, Chemical Society Reviews 37 (2008) 1568–1578.
[2] C. Song, Catalysis Today 77 (2002) 17–49.
[3] S.A. Hajimolana, M.A. Hussain, W.M. Ashri, W. Daud, M. Soroush, A. Shamiri, Renewable and Sustainable Energy Reviews 15 (2011) 1893–1917.
[4] D.A. Noren, M.A. Hoffman, Journal of Power Sources 152 (2005) 175–181.
[5] J.O.M. Bockris, A.K.N. Reddy, Modern Electrochemistry, vol. 2, Plenum Publishing Corporation, New York, 1973.
[6] M. Vogler, A. Bieberle-Hutter, L. Gauckler, J. Warnatz, W.G. Bessler, Journal of the Electrochemical Society 156 (2009) B663.
[7] W.G. Bessler, J. Warnatz, D.G. Goodwin, Solid State Ionics 177 (2007) 3371.
[8] W.G. Bessler, M. Vogler, H. Stormer, D. Gerthsen, A. Utz, A. Weber, E. Ivers-Tiffee, Physical Chemistry Chemical Physics 12 (2010) 13888–13903.
[9] H. Zhu, R.J. Kee, V.M. Janardhanan, O. Deutschmann, D.G. Goodwin, Journal of the Electrochemical Society 152 (2005), A2427.
[10] C. Li, Y. Shi, N. Cai, Journal of Power Sources 195 (2010) 2266–2282.
[11] Ph. Hofmann, K.D. Panopoulos, Journal of Power Sources 195 (2010) 5320–5339.
[12] W.G. Bessler, S. Gewies, M. Vogler, Electrochimica Acta 53 (2007) 1782–1800.
[13] C.J. Moyer, N.P. Sullivan, H. Zhu, R.J. Kee, Journal of the Electrochemical Society 158 (2) (2011) B117–B131.
[14] M. Vogler, A. Bieberle-Hutter, L. Gauckler, J. Warnatz, W.G. Bessler, Journal of the Electrochemical Society 156 (5) (2009), B663-B672.
[15] W.G. Bessler, Solid State Ionics 176 (2005), 997.
[16] K. Vafai, C.L. Tien, International Journal of Heat and Mass Transfer 24 (1981) 195.
[17] Y. Shi, N. Cai, C. Li, C. Bao, E. Croiset, J. Qian, Q. Hu, S. Wang, Journal of the Electrochemical Society 155 (3) (2008) B270–B280.
[18] Y. Shi, N. Cai, C. Li, Journal of Power Sources 164 (2007) 639–648.